A Method of Adapting Three-Dimensional Shock Control Bumps for Swept Flows

Natasha R. Jones[1], Jeremy P. Eastwood[2] and Jerome P. Jarrett[3]
University of Cambridge, Cambridge, CB2 1PZ, UK

Shock control bumps offer the potential to reduce wave drag on transonic aircraft wings. However, most studies to date have only considered unswept flow conditions, leaving uncertain their applicability to realistic finite swept wings. This paper uses a swept infinite-wing model as an intermediate step, and presents a computational study of the design drag performance of 3D bumps. A new geometric parameter, bump orientation, is introduced and found to be crucial to the performance under swept flows. Classic SCBs aligned approximately with the local to freestream flow direction can offer drag reductions comparable to those from similar but un-oriented devices in unswept flows, while badly misaligned bumps see severe performance degradation. For appropriately aligned classic bumps, the relationships between performance and selected geometric parameters (height, streamwise position and isolation) are found to be somewhat similar to those observed in unswept studies.

---

[1] PhD Candidate, Department of Engineering, Trumpington Street, CB2 1PZ.
[2] Department of Engineering. Currently: Technical Lead, DroneDeploy, 474 Bryant Street, San Francisco, CA 94107, USA.
[3] University Lecturer, Department of Engineering, Trumpington Street, CB2 1PZ, Senior AIAA Member.

Nomenclature

b_{edge}, b_e	=	spanwise SCB edge width
$b_{spacing}$, b_s	=	spanwise SCB spacing
b_{width}, b_w	=	spanwise SCB crest width
C_D	=	drag coefficient
C_L	=	lift coefficient
c	=	aerofoil chord length
c_p	=	pressure coefficient
l_{crest}, l_c	=	SCB crest length
l_{ramp}, l_r	=	SCB ramp length
l_{tail}, l_t	=	SCB tail length
M	=	Mach number
Re_c	=	chord Reynolds number
x_c	=	chordwise location of centre of SCB crest
α	=	angle of incidence
δ^*	=	incompressible boundary layer displacement thickness
δ_{99}	=	boundary layer height where velocity is 99% of freestream
θ_r	=	SCB ramp angle
Λ	=	flow direction in x-y plane relative to x-axis
τ	=	SCB shear angle
ϕ	=	SCB isolation ratio
ψ	=	SCB rotation angle
$_{loc}$	=	local value
$_{\infty}$	=	freestream value
$_{n}$	=	projection normal to the wing

I. Introduction

Economic and environmental pressures drive commercial aircraft designers to seek new approaches to drag reduction for transonic wings. Among the numerous concepts, shock control bumps (SCBs) have gained popularity in recent years due to their simplicity of design and operation, and potential to both reduce drag at the design point and reduce separation under off-design conditions.

Early studies focused on 2D SCBs, finding them capable of significant design point drag reductions, typically of 10-20% on aerofoils [1–7]. This arises when the local shock is modified into a lower entropy-creating λ-shock formation [1, 8, 9], and is governed primarily by the SCB height and placement relative to the shockwave. Under off-design conditions the main shock moves over the wing becoming misaligned with the SCB, causing the beneficial λ-structure to deteriorate, and leading to poor off-design performance [3, 10–12].

One promising solution is a closely-spaced array of 3D SCBs, which was first considered in an experimental study by Holden and Babinsky [13]. They showed that, with the correct spanwise spacing, a 3D SCB array could produce an almost 2D λ-shock structure and corresponding control effect, as illustrated in Fig. 1. A further finding was that 3D SCBs produced pairs of streamwise vortices, potentially capable of delaying downstream separation, thus adding benefit in off-design situations. Such findings have been supported by a number of subsequent experimental [7, 10, 14] and numerical [2, 5, 15] studies. The potential for on-design performance similar to 2D SCBs, but with improved off-design performance, has led to 3D SCBs being considered as an attractive means of flow control [16, 17]. This is so not only for aircraft wings, but potentially in engine intakes as well, where the benefit comes from the (2D or 3D) bump's ability to increase the total pressure recovery through shock modification and separation reduction [16–19].

Of the many 3D SCB studies indicating their potential, most have only considered devices placed perpendicular to an unswept flow. The limited number of swept wing studies have instead been more conclusive for 2D bumps, suggesting that both drag performance and optimized shapes are similar to corresponding unswept cases [4, 20, 21]. For 3D SCBs, the design problem increases in complexity; the studies conducted so far thus represent tentative explorations of the design space.

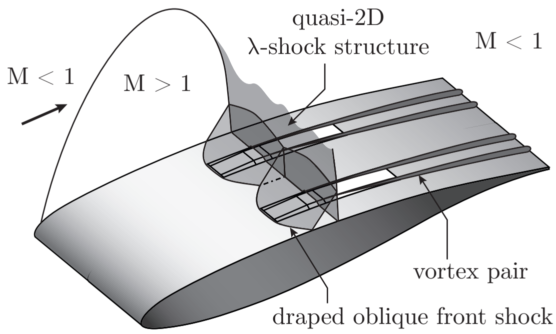

Fig. 1: Flow structures produced by a pair of 3D SCBs as part of an array placed on an unswept transonic wing.

Pätzold et al. [21] optimized single spanwise-truncated 2D SCBs (as if applying a 2D bump to part of a finite 3D wing), and Eastwood [22] analysed a small selection of 3D-SCB arrays. Both used infinite swept wing RANS models, and set their SCBs normal to the wing leading edge (LE). Both also demonstrated difficulty achieving similar levels of drag performance to those observed in unswept flows; the latter showed that achieving some off-design benefit was still possible. In order to better understand the possible utility of 3D devices for realistic aircraft applications, further swept wing investigations are required, including the examination of both on- and off-design performance.

In considering swept flows, one important new question is how a 3D SCB should be oriented on the wing. Since the classic and well-studied symmetrical flow-field from unswept studies is rendered unattainable by boundary layer crossflows and the chordwise (and for 3D wings, spanwise) variation of the local flow direction Λ_{loc}, it is sensible to consider orientations away from the LE-normal. The SCB could be aligned with Λ_{loc} at some specified location, but the presence of the bump is likely to affect the local flow direction, making the prior determination of the correct angle challenging. Furthermore, while an SCB set at an arbitrary angle to the flow is still likely to be able to generate some level of drag reduction [21, 22], the viscous interaction important for the off-design performance is likely to be more complex.

A. Questions

The addition of sweep and orientation variables significantly complicates the design of a 3D SCB array. This paper seeks to address two of the principle questions that arise.

For SCBs in swept flow:

1. do the trends observed in unswept flows that relate performance and geometry still hold?

2. how does orientation influence their performance?

B. Experiment Design

To answer these questions, ideally a comprehensive study of the expanded design space would test the interplay between sweep, orientation and the existing geometry. However, the resources available to any realistic investigation make such an exploration prohibitively expensive. Instead, a parametric experiment must be carefully designed to offer useful but directed conclusions.

To achieve this, this paper makes two important decisions. Firstly, the study of SCB geometry will be bounded by considering only those general shapes classically used in unswept studies. Much is already known about these well-studied geometries, providing a useful benchmark of performance and behavior. Secondly, the questions stated above will be addressed in reverse order.

This enables the new, unknown influence of orientation and its effect on swept performance to be dealt with first, without the complication and additional cost of including the SCB geometry. An optimal orientation is sought for one typical and one less typical unswept SCB design. This then leads into the study of SCB geometry, which uses the proposed optimal orientation of the typical SCB as an adaptation method for swept flows. If the method is sufficient, then the rotated SCBs would show maximum performance similar to those in unswept flow. This is tested through examining the influence of key design variables. To retain a practical scope in this paper, the list of geometric variables tested is limited to those which are already known to be crucial to the performance of unswept 3D SCBs: position (eg: [1, 2, 6, 10]), height (eg:[2, 3, 6, 8]), and isolation [2]. While other parameters undoubtedly also have influence, detailed investigations are not considered here.

The results are preceded by a description of the SCB parameterization and computational model, and followed with a discussion of the study's limitations and the conclusions.

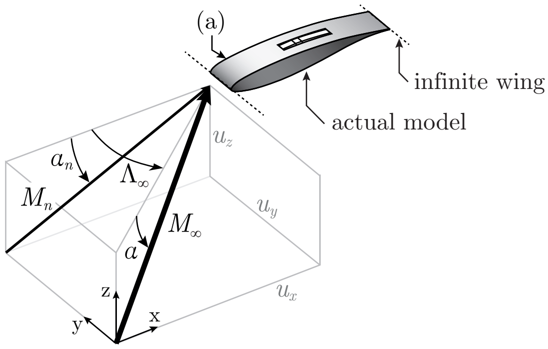

(a) Definition of swept flow.

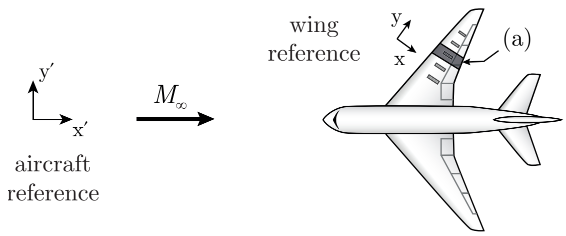

(b) Infinite wing model in relation to an aircraft.

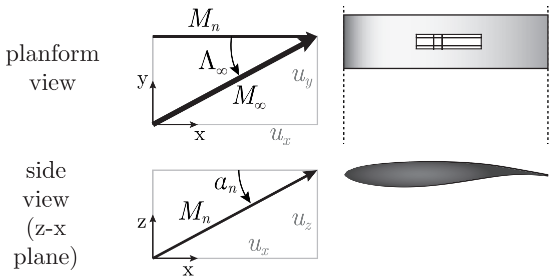

(c) Orthographic projections of model.

Fig. 2: Definition of infinite wing and flow model.

II. Infinite Swept Wing Model

A. Aerofoil Model Definition

While a full 3D aircraft model would be the ideal test configuration for a swept flow investigation, the parametric design study presented here contains $O(10^2)$ analyses, rendering this far too computationally expensive. An infinite-wing model is the next-best alternative, and here the OAT15A turbulent supercritical section is used as the baseline aerofoil [23]. The flow model according to simple sweep theory is shown in Fig.2, with freestream conditions defined by Mach number M_∞, sweep angle Λ_∞, and incidence α. The LE normal components are $M_{\infty,n} = M_\infty \cos\Lambda_\infty$ and $\alpha_n = \tan^{-1}(\tan\alpha/\cos\Lambda_\infty)$. These, rather than the freestream values, define the fixed test condition of the aerofoil, enabling comparisons between swept and unswept cases with equivalent LE-normal c_p distributions. Increasing Λ_∞ is therefore equivalent to adding a spanwise flow.

As mentioned, other SCB studies have used a similar model [4, 21]. Those authors highlighted that, while simple sweep theory may be appropriate for laminar incompressible flow, for turbulent compressible flow the principle of independence between chordwise and spanwise components no longer necessarily holds. Inherent 3D mixing results in an increased boundary layer displacement and a small reduction in effective camber of the aerofoil [4, 21]. Similarly, in compressible flows density variations depend on both chordwise and spanwise velocity components, which again has particular significance for boundary layer development [24], though provided the freestream Mach number and sweep are moderate enough, the two directions can be considered sufficiently uncoupled [25, 26]. The results of [4, 21] suggest these effects have little impact on the optimization or performance of 2D SCBs, and therefore that the swept flow model is suitable.

Since the lift and drag coefficients are evaluated in the direction of the freestream flow, an approximate relation of $C_{L,\Lambda} = C_{L,\Lambda=0} \cos^2 \Lambda_\infty$ exists between the swept and unswept lift values. The drag coefficient varies with sweep according to the balance of the decreasing pressure drag and increasing viscous drag. Also note that the Reynolds number in the direction of the freestream now follows the relationship $Re_\Lambda = Re_{\Lambda=0}/\cos^2 \Lambda_\infty$. To simplify comparison between the two flows, performance results are later expressed as percentage changes relative to the respective clean-wing flows, removing the issue of differing absolute values.

B. SCB Geometry Definition

The classic SCB shapes of unswept studies can be mostly placed into two catagories, smooth contour bumps and wedge bumps, within which there are many variations. Here, for ease of computational design, the rectangular wedge profile is used, parameterized as indicated in Fig. 3. A default geometry is defined in Table 1; values were selected to give a typical wedge shape. To reduce the number of free variables as discussed, the SCB lengths are fixed. These were chosen based on [2], which suggested $l_{ramp} = 0.1c$, $l_{tail} = 0.2c$, and a pointed crest, giving a $l_{total} = 0.3c$. However, a flat crest is desirable to reduce the severity of flow re-expansions there [17]. A typical value of $l_{crest}/l_{total} \approx 13\%$ was obtained from [27], giving $l_{crest} = 0.04c$. Then l_r and l_t were shortened equally to keep the crest center at 33% of l_{total}. All this means SCB height is solely controlled by θ_r. The SCB position x_c is defined as the distance from the wing LE to the centre of the crest,

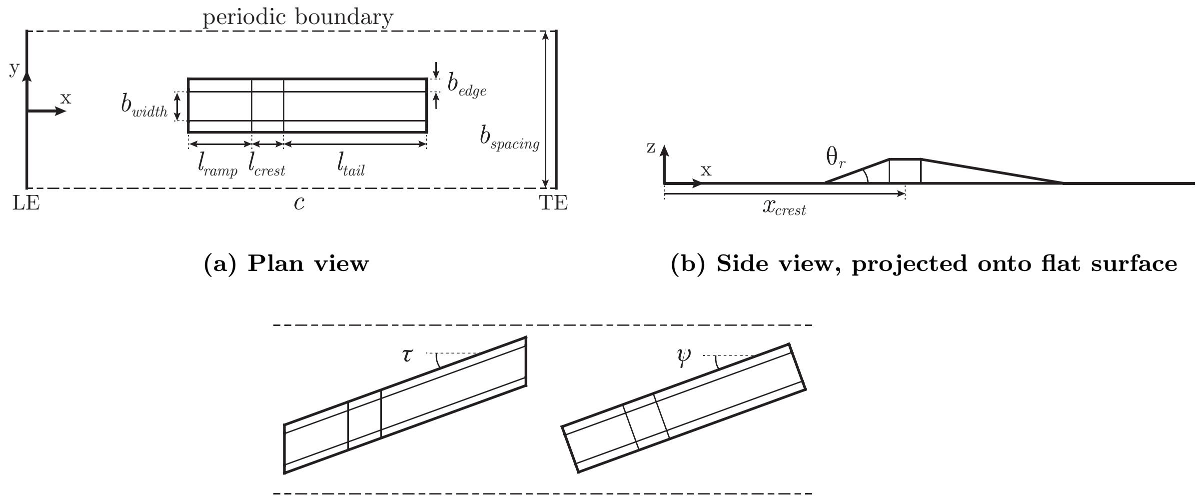

(a) Plan view

(b) Side view, projected onto flat surface

(c) Possible orientation definitions

Fig. 3: 3D SCB geometry parametrisation

along the chord in the wing-normal (x) direction. The default x_c value is discussed in Section II E.

The spanwise geometry prior to altering orientation is defined in Fig. 3a. The default values of b_{edge} and b_{width} produce a design similar to many tested in CFD and tunnels: narrow-edges (eg: [2, 10]), and fairly high aspect ratio (here a little higher than [17]). The domain (mesh) width determines the SCB spacing. The default value of b_s, combined with b_w, gives the default SCB a high isolation [2], which allows large changes to orientation without risk of the bump crossing the periodic boundaries. The values in Table 1 can be assumed later in the paper unless otherwise stated.

The SCB orientation (Fig. 3c) is applied last to the 3D SCB. For the present work, a simple rotation of angle ψ is used; this retains the most similarity with unswept SCB shapes, and is defined using a standard 3D transformation matrix:

$$R_\psi = \begin{bmatrix} \cos\psi & -\sin\psi & 0 \\ \sin\psi & \cos\psi & 0 \\ 0 & 0 & 1 \end{bmatrix} \tag{1}$$

where the centre of the crest defines the pivot. This definition has some disadvantages: for example, as ψ increases the proportion of the wing-normal chord covered by the SCB decreases. An alternative transformation which avoids this might be a simple shear of angle τ, however this has its own

Table 1: Fixed ( ) or default (*) values of SCB parameters

l_{ramp}	l_{crest}	l_{tail}	x_c*	b_{width}*	b_{edge}*	$b_{spacing}$
$0.08c$	$0.04c$	$0.18c$	$0.48c$	$0.04c$	$0.01c$	$0.40c$

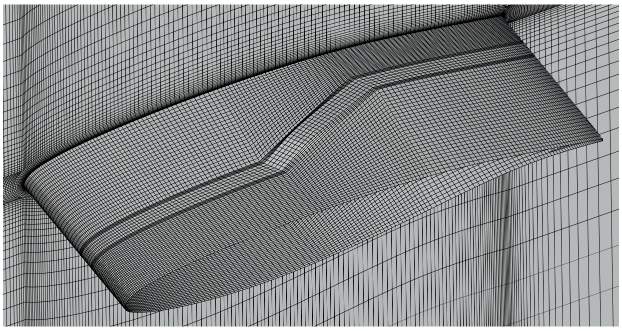

Fig. 4: Typical SCB mesh ($b_{edge} = 0.01c$, $\psi = 28°$.

downsides, eg: as τ increases, the SCB's edges become steeper as viewed perpendicular to themselves. Although features such as these are undesirable, it is clear that no orientation definition would eliminate all such problems, and for this reason, rotation is the choice in this study.

The final 3D profile is added conformally to the aerofoil surface, with the edges formed as linear extrusions down to the clean wing surface. The major advantage of this definition is that when $\theta_r = 0°$ the original surface is retained. Since the SCBs adopt the curvature of the underlying aerofoil surface, different designs may obtain different curvatures. While the impact of this is neither well established nor easy to assess, with variations in both orientation and streamwise placement, a non-conformal definition would be inappropriate.

C. CFD Model

The mesh is a structured O-H grid generated in IcemCFD, with 334 surface nodes in the chordwise plane, leading and trailing edge spacings of approx. $0.2\%c$, and both spanwise and streamwise maximum spacings of $1\%c$. A few additional node lines are added along the SCB edges to improve resolution of the flow gradients. The boundary layer O-grid contains 30 surface-normal nodes and gives a cell wall distance of $y^+ < 1$ everywhere. To accommodate a swept flow, periodic boundary conditions are applied at the spanwise extremes.

The mesh's chordwise boundary, at which a pressure far-field condition is imposed, extends $20c$ upstream, above and below, and $40c$ downstream of the aerofoil. It is recognized that the extent of the far-field (FF) does not guarantee total independence from boundary influence. Therefore additional (2D), tests are presented in Fig. 5b to quantify this influence, using grids with the FF extended to $50/80c$ and $100/150c$. The results show a small shift (decreasing C_D) in the drag polars, which remain within the range of experimental data. Whilst some FF influence is not strictly ideal, such a trade-off between domain-size and computational cost is necessary, and one which should not interfere with later results: of interest are the relative performance trends obtained at a fixed test condition, rather than absolute values.

To retain the geometry definition when SCBs are rotated, the blocking structure is fitted to the bump edges. The maximum node spacing constraint leads to a greater number of spanwise nodes for rotated SCBs. For example, a mesh with $b_{spacing} = 0.4c$, $\psi = 0°$ has approx. 2.1 million nodes, or with $\psi = 30°$ approx. 3.0 million nodes. While this is fairly coarse, it is necessary to facilitate a large number of parametric tests. An example of a typical mesh is shown in Fig. 4.

D. CFD Solver

The software used is ANSYS Fluent v15.0, a finite volume code for both 2D and 3D simulations, using the implicit density-based RANS solver [28]. Second order spatial discretisation is used for all equations. The selection of a turbulence model is investigated as part of the validation tests presented later in Section II F. A convergence acceleration technique known as solution steering is available in Fluent and was used to full effect, allowing the software to determine step increases in CFL from 1 up to a maximum of 100 towards the end of the simulation. Cases are either 'cold' or 'warm' started. A 'cold-start' uses Fluent's FMG initialization method, (giving an initial guess with residuals of approx. $1e^{-1}$ lower than other options). Simulation times depend on mesh size; as an example, a mesh with $b_{spacing} = 0.4c$, $\psi = 0°$ took approx. 12 hours to converge. A 'warm-start' uses previously converged solution data from a compatible grid, whenever available, to reduce computation times by up to 2/3.

Convergence was assessed using C_L and C_D, with a stop criterion of $\leq 0.005\%$ variation in each over the last 20 iterations. For cold-start cases, this coincides with reductions of all residuals of $\sim 1e-6$. For warm-start cases initialized with data from very similar geometry, (typically $\Delta\theta_r = \pm 1^\circ$), further changes in the solution are relatively small, and convergence of lift and drag forces are achieved much before further reductions in residuals of $1\mathrm{e}^{-6}$, making the former a more appropriate and efficient appraisal.

Simulations in the parametric tests are run using serial Fluent on a quad-core machine with 3.4GHz CPUs, with maximum available RAM of 16GB.

E. Test Condition

The selected test condition for the study is $M_{\infty,n} = 0.71$, $\alpha_n = 2.50^\circ$, $Re_c = 7.2 \times 10^6$, with $\Lambda_\infty = 30^\circ$ (giving $M_\infty = 0.82$). This was chosen to match data for swept half-wing-body models based on the OAT15A [29], facilitating possible future increases in model fidelity. A fixed incidence is used (as in [21]), as opposed to the more conventional fixed C_L, to reduce computation times by obviating the need to iterate through multiple incidences per solution. Whilst this then does not remove the ability of the shock to move due to boundary layer effects (Section II A), the resulting displacement on the clean wing was observed to be at most 1%c, and should therefore not have significant impact on the parametric test results (see Section IV A).

The selected clean-wing α_n gives a high C_L (0.954 in the present computations) and aft shock position ($x_{sh} = 0.46c$). This test condition is thus reasonably close to the computationally-predicted buffet boundary, again anticipating future work considering the off-design SCB performance. Limited work on unswept [30] and swept [20] infinite-wings has suggested that SCBs positioned aft on the aerofoil (possibly entirely behind the shock [20]) have better (though not necessarily good) buffet characteristics. Since an aft-placement (for SCBs not completely post-shock) implies a higher drag design-point C_L, such an approach was adopted here.

The SCB is placed by default at $x_c = 0.48c$ (Table 1), to match the general recommendation in the literature that SCBs perform best when the shock is 1-3%c in front of the crest [1, 2, 6]. In practice, of course, the presence of an SCB may alter the shock position.

F. Validation

To verify the suitability of the meshes, both grid refinement and turbulence model studies have been performed. Both are conducted first using a 2D clean-section mesh (ie: chordwise plane), and then the grid refinement is additionally checked for a 3D SCB mesh. In these tests, pressure distributions are compared to computational data from Deck [31] and experiments by Jacquin et al [32] at $M_{\infty,n} = 0.73, \alpha_n = 2.50°$, $\Lambda = 0°$, $Re_c = 3 \times 10^6$. Drag-polar data are compared to experiments in two ONERA wind tunnels by Rodde and Archambaud [23] at $M_{\infty,n} = 0.73$, $\Lambda = 0°$,$Re = 6 \times 10^6$. The present work is conducted at slightly different Reynolds numbers of $Re_c = 3 \times 10^6$ and 7.2×10^6, the latter being the value used in the rest of this paper.

For the mesh study in 2D, the standard grid node spacing (Section II C) was divided by $1/\sqrt{2}$, $\sqrt{2}$, 2, and $2\sqrt{2}$ in all directions, forming five grids in total. These were tested using the Spalart-Allmaras (S-A) turbulence model, a preliminary selection made due to its suitability for wall-bounded external flows [33]. Results for the standard grid are compared to the literature data in Fig. 5. The other grids are not shown because of the very close overlap with this data; the only notable difference in c_p distributions was an expectedly sharper shock resolution on the finer grids. The match with the other CFD case by Deck [31] (also with the S-A model) is good, although neither match the experimental shock position; this is a typical problem with CFD to wind tunnel comparisons.

Mesh-independence of the lift and drag forces is also important. The 2D grids all produced similar values, but the standard grid did not quite reach the mesh-independent values. The errors were small however, at about 1% in C_L and C_D, and 0.2% in L/D; to obtain these required the mesh with four times as many nodes.

The mesh resolution was also checked in 3D, focusing on the spanwise node spacing which cannot be tested in 2D. This geometry included a SCB of $\theta = 3°$, $\psi = 0°$, $b_{spacing} = 0.1c$ and otherwise default parameters. A sequence of four meshes was built in a similar manner, dividing the node spacings by $1/\sqrt{2}$, $\sqrt{2}$, and 2. However for the finest grid, only the spanwise spacing is increased above the previous mesh, due to the size limits imposed by the available computational resources. Fig. 6 shows the changes in C_L, C_D and L/D relative to the standard grid for these 3D meshes.

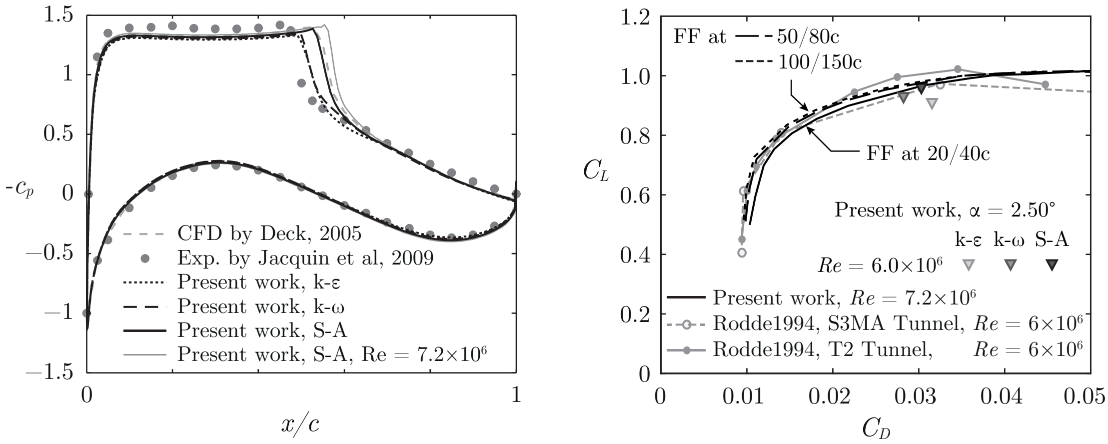

(a) c_p distributions (all $Re = 3 \times 10^6$). **(b) L-D polar.**

Fig. 5: Comparison of standard 2D grid with experimental data by Jacquin et al [32], Rodde and Archambaud [23] and computational data by Deck [31].

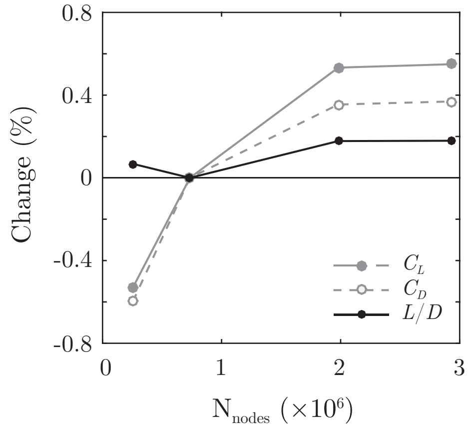

Fig. 6: Comparison of force predictions versus mesh size for 3D SCB section.

Again the standard grid does not quite reach mesh independence, but the differences are small, at about 0.5%. It was therefore decided that the standard grid represented a suitable trade-off between accuracy and computation time, which increases approximately in linear proportion to the mesh size.

The turbulence model test therefore used the standard grid, in 2D, and compared three of the models available in Fluent: S-A, SST k-ω, and k-ϵ. Fig. 5a shows all three predict similar c_p distributions except near the shock; the k-ϵ and SST shocks are further forward, associated with lower C_L predictions than the S-A case (similar to results by Brunet [34]). The k-ϵ model also fails to predict the small post-shock separation bubble mentioned by [31, 32], showing higher post-shock pressures and positive streamwise wall shear stress (not presented), whereas the other two models do show these features. While the pressure plot with the k-ω model matches the experimental case slightly better, the *L-D* results in Fig. 5b suggest the S-A model as the closer match with the expected trends. Overall it is reassuring to see similar results between the two models. The L-D polar at $M_{\infty,n} = 0.73, \Lambda_\infty = 0°$ was completed with the S-A, and is shown in Fig. 5b to match reasonably well with Rodde and Archambaud's data, even without considering the small Re_c difference and the scatter in the experimental data. Towards the right-hand edge of Fig. 5b the drop-off in C_L is somewhat under-predicted, but in these highly-separated flow regimes such a deviation is unsurprising in RANS results.

Therefore, based on the *L-D* results, and the understanding that no turbulence model is likely to predict accurately separation and reattachment (which are important when aerofoils or aircraft wings operate at the extreme end of their flight envelopes), the remainder of the present paper continues with the S-A model. As a conclusion from both the mesh and turbulence tests, the 2D and 3D meshes and solver settings appear to be reasonably well validated for both the clean and modified (SCB) aerofoil sections.

III. The Effect of Orientation

A. Orientation Hypothesis

Before investigating orientation, it is worth considering factors which might influence, and enable some prior estimation of, an optimal setting angle for the default, classic SCB.

One obvious choice of alignment would be with the freestream (here $\Lambda_\infty = 30°$). Pätzold et al [21] noted local variations in L/D over the edges of spanwise-finite 2D SCBs oriented perpendicular to the wing LE (ie: $\psi = 0°$). By aligning the SCB with the drag vector, its edges contribute no wetted area to the force integral.

However, near the surface the spanwise flow component is not uniform, with the local flow direction Λ_{loc} both differing from the freestream value, and varing along the chord. The pressures

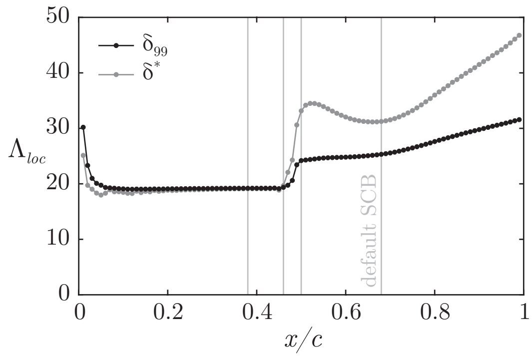

Fig. 7: Local flow direction as a function of chordwise distance ($M = 0.71$, $\alpha = 2.50°$, $\Lambda_\infty = 30°$

on each side of the SCB will increase or decrease locally depending on the orientation ψ relative to Λ_{loc}, causing a pattern of re-expansions and compressions. This is generally undesirable, as such features might strengthen the main shock and/or encourage earlier breakdown to a double shock system; this is also likely to be worse for typical 3D SCBs with narrow edges. Fig. 7 plots Λ_{loc} against two measures of the boundary layer thickness, with he default SCB ($\psi = 0°$) location indicated. Over the ramp, Λ_{loc} is roughly constant at 20°, while post-shock and over the tail it is higher at $25 - 35°$. The following alignments could then be proposed:

- $\psi = 30°$ - freestream
- $\psi = 20°$ - to best reproduce the unswept ramp flow, and mitigate re-expansions over the pre-shock leeward edge [22]
- $\psi = 25 - 35°$ - to match the tail flow, alleviating re-expansions over the post-shock windward edge
- $\psi = 23 - 29°$ - a estimate of average Λ_{loc} along the SCB: since it is impossible to match both the pre- and post-shock values using a parallel-sided SCB, this represents a compromise

The presence of the bump is, of course, likely to affect the local flow direction, complicating the prior determination of an alignment that achieves any stated aim.

Two further points should be noted, though they are beyond the scope of this study. Firstly, since the spanwise flows inevitably cause the bump edges act partly as a ramp or tail, spanwise-asymmetric designs could considered: for example, unequal edge widths, or curved SCBs (eg: following local streamlines). Secondly, the viscous interaction may also influence the choice of orientation. Recent findings [27] suggest that the ramp is responsible for the production of the vortex pair in Fig. 1. If this also holds for swept flows, and it were desirable and possible to mimic the unswept vortex pattern, aligning the ramp with its local flow might offer the means to do this. It is also uncertain as to whether the optimal alignment for on- and off-design performance would coincide, or if a trade-off would be involved in selecting orientation.

B. Rotated SCBs

To begin assessing the effect of orientation, the default SCB is tested with varying θ_r as follows:

- $\Lambda_\infty = 0°$, $\psi = 0°$ (as a benchmark)
- $\Lambda_\infty = 30°$, $\psi = 0, 20, 30, 40, 50°$

Fig. 8 presents these results as percentage changes of $\Delta L/D = (L/D_{scb} - L/D_{clean})/L/D_{clean}$ at each flow condition (Section II A).

For the unrotated SCBs, and similar to results obtained by [22] on a different aerofoil, the SCB under swept flow sees: reduced performance for any given θ_r; a lower maximum performance, L/D_{max}; and a smaller corresponding optimal ramp angle, θ_{max}. Comparable to the unswept case, beyond θ_{max} the beneficial λ-structure breaks down into a skewed double-shock system, beginning in the proximity of the SCB; this just begins earlier in the swept flow. Observed in c_p contours for

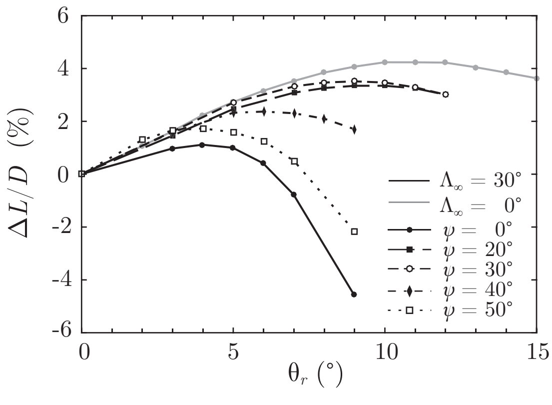

Fig. 8: Performance of rotated SCBs under swept ($\Lambda_\infty = 30°$) flow.

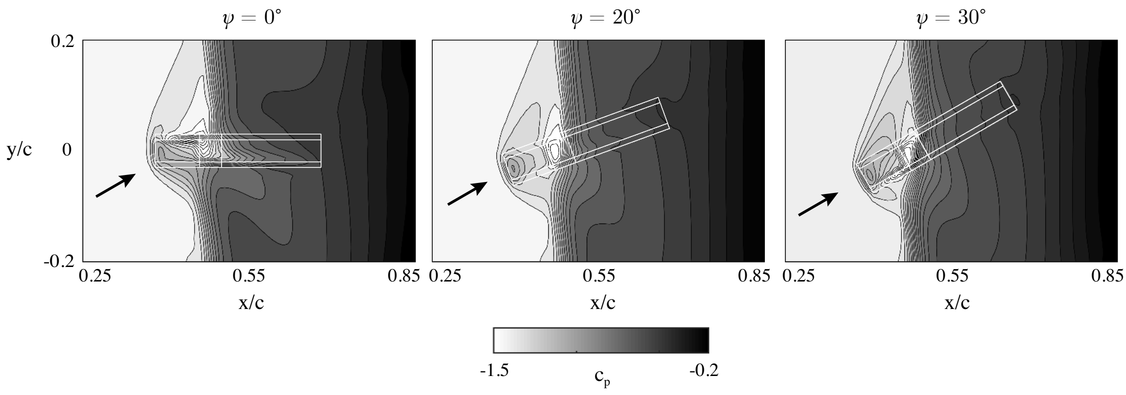

Fig. 9: Surface c_p plots comparing SCBs of $b_{edge} = 0.01c, \theta_r = 7°$ and different rotations, under swept 30° flow (flow moves diagonally upwards, from left to right).

$\theta_r = 7°$ in Fig. 9 are: a strong re-expansion over the leeward side, ahead of and locally strengthening the main shock; re-expansion over the windward edge behind the shock; higher pressures in the λ-region on the windward side. These features are likely to encourage deterioration of the λ-structure, and hence be responsible for the adverse performance trend. There are also suggestions of separation behind the leeward crest/edge, but this should be verified with more appropriate CFD tools and/or wind tunnel experiments.

Rotated SCBs however show much improved performance. The two rotated examples in Fig. 9, despite having $\theta_r = 7°$ like the unrotated one, operate just below their maximum performance, and shock-detection algorithms do not yet indicate λ-shock breakdown. Fig. 9 suggests that using $\psi = 20 - 30°$ does reduce the severity of re-expansions around the SCB induced by the spanwise flow, as postulated in Section III A. Further, the $\psi = 20°$ SCB does appear to have an almost symmetrical ramp flow. However, the $\psi = 30°$ bump, despite seeing some flow re-expansion now on the opposite sides to those of the unrotated SCB, performs slightly better for most θ_r, which suggests that the ramp flow alignment is not the optimal choice.

As with all RANS investigations, some doubt should be cast on the ability of the numerical codes to accurately capture the post-shock viscous flow. Hence in this study, focus is on the upstream flow over the ramp/crest, which is responsible for much of the benefit provided by the SCB [27].

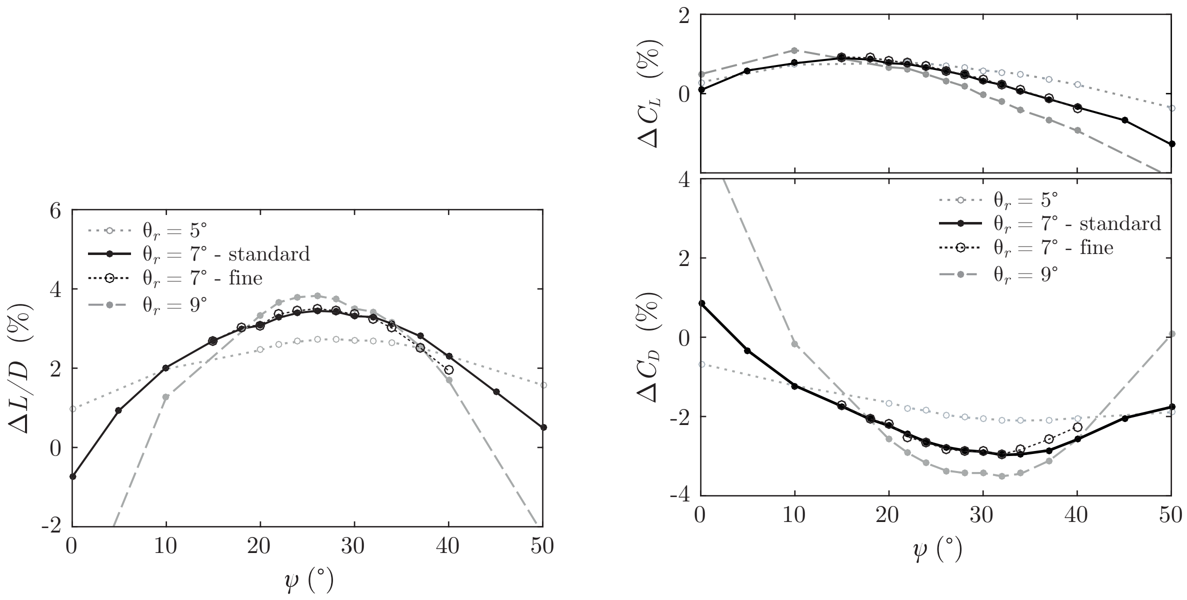

(a) L/D **(b)** C_L **and** C_D

Fig. 10: SCB performance against rotation ψ.

C. Optimal Rotation Study

To make a better assessment of the optimal orientation, ψ_{opt}, a finer-resolution study of ψ is needed.

Firstly though, it is clear from Fig. 8, that the influence of ψ depends on θ_r. At low θ_r, there is less variation in performance between SCBs of differing ψ; however to achieve optimal performance, θ_r must be high, under which circumstances there is clearly a preferable orientation. Thus to determine ψ_{opt} a reasonably high θ_r is needed. Using $\theta_{max} = 9°$ (based on $\psi = 20, 30°$) would satisfy this. However, for this θ_r, SCBs with low or high rotations ($\psi \sim 0, 50°$) have strongly adverse performance, and so doubt in the RANS results of such cases would not be unfounded. A lower $\theta_r = 7°$, giving close to peak performance (and matching Fig. 9), is therefore the initial choice, with additional points for $\theta_r = 5, 9°$ filled in only near ψ_{opt}. For efficient use of computational resources, a small interval $\Delta\psi = 2°$ is used to resolve the peak, with larger intervals elsewhere.

Fig. 10a shows that for $\theta_r = 7°$, $\psi_{opt} = 26 - 28°$, equivalent to being slightly toed-out on the wing, with a fairly broad performance peak between $\psi = 22 - 32°$. For $\theta_r = 9°$, the peak is narrower and higher, between approx. $\psi = 24 - 28°$, with $\psi_{opt} = 26°$. For $\theta_r = 5°$, it is broader and lower, around $\psi = 20 - 37°$, with again $\psi_{opt} = 26 - 28°$. Increasing SCB ramp angle (and so height) has little impact on ψ_{opt}, but does increase the sensitivity of performance to ψ. The value of ψ_{opt} and the broader peak do appear to represent a middle ground (or average local flow) which moderates the spanwise flows over the length of the SCB, ensuring that no part of the SCB sees particularly strong re-expansions.

To confirm the accuracy of the identified trends, selected tests have been repeated using finer grids. The chosen tests are those near ψ_{opt} ($\psi = 15 - 40°$) for $\theta_r = 7°$, plus the corresponding swept, clean-wing case. The grids were produced by dividing all node spacings by $\sqrt{2}$; as indicated by Fig. 6, this should give mesh independent results. Resulting SCB grid sizes ranged from 7-9 million nodes, so had to be run in parallel Fluent, split over 8 nodes of a computing cluster. Each case was initialized by interpolating the existing solution data onto the finer grid; depending on mesh size, each took around a day to achieve convergence of lift and drag forces.

These additional tests, also plotted in Fig. 10a, support the results discussed: the fine-mesh cases overlap strongly with the other data, affirming the optimal rotation and shape of the peak. Somewhat larger deviations in performance are observed at the highest rotations $\psi \geq 37°$, amounting to a difference in $\Delta L/D$ of -0.35% at $\psi = 40°$. This increasing divergence is likely due to slowly deteriorating mesh quality, but since the important values and trends are confirmed, this is not of great concern.

On account of using a fixed-α and not fixed C_L test condition, individual plots of ΔC_L and ΔC_D are shown in Fig. 10b, to verify that performance improvements are not entirely due to a change in C_L when the SCBs increase effective camber. The plots clearly show this ($|\Delta C_L| < |\Delta C_D|$). ΔC_L is of course not constant with ψ, due to a combined influence from small variations in local effective camber due to the SCBs with changing θ and ψ, along with a streamwise blockage effect at low or high ψ, due to the steep edges. Such sectional variations in L/D on wings with 3D bumps are expected, and seen in slight distortions of shock fronts, such as in Fig. 9, and are likewise observed in unswept-cases. Performance at high or low ψ is clearly worse due to poorer drag performance, particularly for tall SCBs. In the mid-range of ψ, around the 'peaks', C_L falls slightly whilst C_D is relatively flatter, hence taking ψ_{opt} from L/D gives a value at the lower end of that range. All three drag curves again exhibit roughly the same optimum and the same relative sensitivities to ψ.

D. Factors Influencing SCB Alignment

Having established an optimal alignment for the default classic SCB, it auspicious to note some additional factors that might affect its value for this and other bump designs. These arise from changes to the apparent SCB geometry, as experienced by the oncoming flow, due to the changing orientation. Possible influences on ψ_{opt} can therefore be summarised as:

- spanwise flow interaction with edges - Section III A
- 'effective tail geometry' (consequence of edge design) - likely to impact the boundary layer and any potential tail/downstream separations (as may occur in unswept flows [10, 14, 27, 35])
- 'effective ramp angle' felt by oncoming flow - since edges are typically steeper than the ramp; but studies decoupling the effects of θ_r, l_{ramp} and SCB height are lacking (to the authors' best knowledge).
- 'effective isolation' - wider or more closely spaced 3D SCBs are more like 2D SCBs, having a higher $/D_{max}$ at a smaller θ_{max} [2]. They affect more of the oncoming flow, less of which is able spill sideways off the ramp. Rotation may affect how isolated SCBs appear to be.
- geometric effects - for example, ψ affects the chordwise location of the ramp's start-line, which also becomes non-uniform. This might affect the size of the draped, skewed λ-region.

E. Wide-edged SCB

Of the possible factors mentioned in the previous section, the interaction of the spanwise flow with the default bump's steep edges can be more easily eliminated, and it is of interest to do so in order to make an exploratory assessment of how important the SCB edges are in swept flows, and whether they do indeed determine or influence the optimal orientation.

A wide-edged design is therefore introduced with $b_{edge} = b_{ramp} = 0.08c$ (Fig. 11). This particular value of b_e also attempts to ameliorate changes in the effective ramp angle due to rotation,

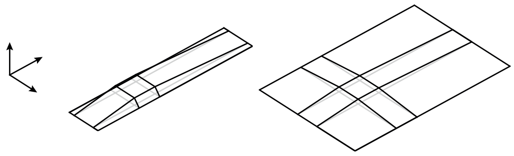

Fig. 11: Isometric view of narrow- and wide-edged SCBs.

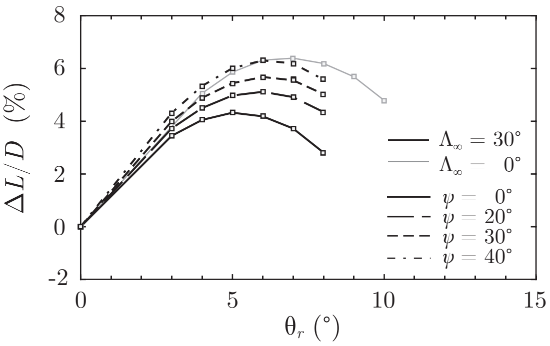

Fig. 12: Performance of wide-edged SCBs.

though of course with a rectangular SCB planform, changes in turning angle over the edges cannot be eliminated entirely.

The SCB is tested in the same manner as that in Section III B, for comparison with the narrow-edged SCB. $\psi = 50°$ is excluded, since the SCB edges approach the domain boundaries, creating excess skew in the mesh, and causing doubt about the accuracy of RANS. As an indicator of mesh quality, the worst case ($b_e = 0.08c$, $\psi = 40°$) has a maximum equiangle skew of 0.814 (scale: 0 good, 1 degenerate), which is toward the limit of acceptability [36], with 6% of cells having skew above 0.5, and 0.61% above 0.75. The minimum orthogonal quality is 0.032, with $< 0.1\%$ of cells below 0.2.

From Fig. 12, the unrotated case suffers performance degradation under swept flow similar to the previous narrow-edged design. The relative reduction, however, is somewhat less for the wide-edged bump, which suggests a more moderate interaction between the wide sloping edges and the spanwise flow. Limited swept tests in [21], on spanwise-truncated 2D SCBs with two different edge widths ($0.1c$ and $0.05c$), also showed such differences, with more severe local L/D fluctuations for their narrower-edged case.

For rotated cases, similarities are observed between Figs. 12 and 8. The curves are of the

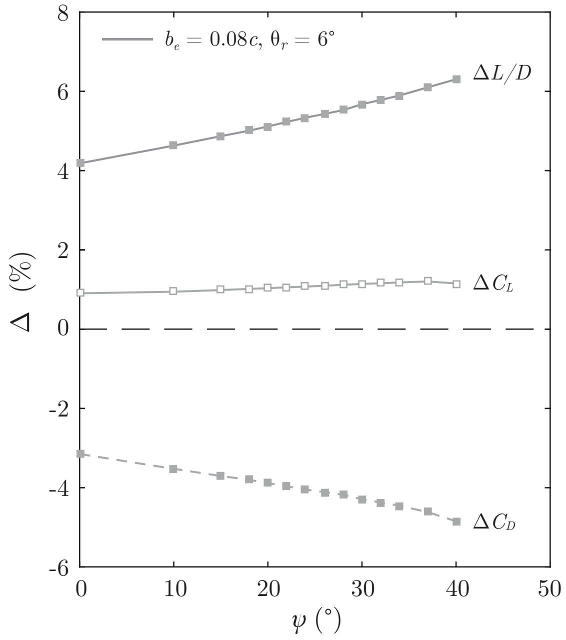

Fig. 13: Optimal rotation study for wide-edged SCB, $\theta = 6°$.

expected shape, though since the wide-edged bump is generally less isolated than the narrow-edged design, it has lower values of θ_{max} [2]. Shorter SCBs are again less sensitive to ψ, (eg: $\theta_r = 4°$ vs $6°$).

The significant difference is that the wide-edged SCB does not have quite the same behavior with respect to rotation. Instead, between $0 - 40°$, increasing ψ keeps improving performance. The plot of ψ_{opt} in Fig. 13 further illustrates this, filling in the gaps for the $\theta_r = 6°$ bump (which is θ_{max} for $\psi = 20 - 40°$).

The question is then what causes the different behaviour regarding ψ_{opt} and sensitivity to ψ. Firstly, it can be reasonably concluded that the significance of the edges is reduced in this case. Since the edge steepness is determined both by b_{edge} and by θ_r, which controls the SCB height, a larger b_e combined with lower θ_r's weakens the detrimental interactions between the edges and spanwise flows observed in Section III B. With the role of the edges diminished, the influence of other factors on the rotation-performance relationship should now appear more prominently.

For this SCB with wide sloping edges, it might be supposed that from Section III D the new dominating influences would be isolation, and other geometric effects. The latter would be considered due to the large planform of the wide-edged SCB, which means that rotation would affect the chordwise coverage of the ramp far more than with the narrow-edged, and narrow-overall default SCB. Such effects are however difficult to quantify.

That changes in effective isolation play a part can be demonstrated via a thought experiment. The wide-edged SCB at $\psi = 0°$ has a total width of $0.2c$. If rotated to $\psi = 90°$, it would become equivalent to a short-tailed, asymmetric-edged bump with $\psi = 0°$ and total width of $0.3c$. Thus at $\psi = 90°$ the bump would appear more like a 2D case (under unswept flows at least), and so be expected to have a higher L/D_{max} and lower θ_{max} compared to low-ψ cases. If Fig. 13 could be continued to $\psi = 90°$, reduced performance should be observed, since at high rotation the value of $\theta_r = 6°$ would be above θ_{max}. Some value of ψ_{opt} should then exist above 40°. This could also be why the $\psi = 40°$ SCB in Fig. 12 outperforms the unswept case at some values of θ_r. As said, a slightly higher L/D at lower θ_{max} is suggestive of isolation effects. There could also be some contribution from a poorer mesh quality as ψ increases.

Again, plots of ΔC_L and ΔC_D are added to Fig. 13 to show that the performance of the wide-edged SCBs is not solely due to increasing C_L due to increasing effective camber. The variation of C_L is small, with SCBs of $\psi = 0 - 40°$ all having approx. the same C_L, and again $\Delta C_L < \Delta C_D$.

IV. Geometry and Performance Trends in Swept Flows

The previous section showed rotation to have a significant effect on the drag-performance of SCBs. The optimal alignment of the default narrow-edged SCB appears to match an average local flow direction in the vicinity of the bump, according to the considerations in Section III A, whilst other factors appear more important for less typical wide-edged designs. This investigation now turns to performance design trends, and asks how well those from unswept flows hold for optimally-rotated SCBs in a swept flow. Since this is a large problem, only SCBs with more typical narrow-edges are considered, and the associated ψ_{opt} of $26 - 28°$ is proposed as an adaptation method. Therefore, additionally of interest is whether this is effective in obtaining bump designs of similar performance and behavior, or if further considerations are required.

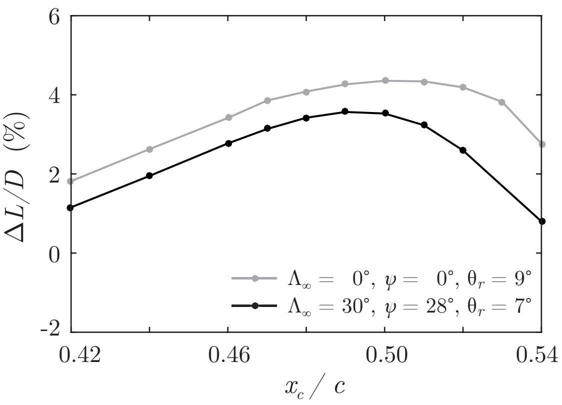

Fig. 14: Chordwise placement versus performance for two SCBs.

A. Chordwise Position

One of the most important influences on the drag performance of SCBs in unswept flow is their chordwise position relative to the shockwave. To check for similar behavior in swept flow, two comparably performing SCBs are selected: for $\Lambda_\infty = 30°$, $\theta = 7°$ (as in Figs. 9, 10a) and $\psi = \psi_{opt} = 28°$ (according to Fig. 10a, the choice between 26° and 28° is unimportant for this design); for $\Lambda_\infty = 0°$, $\psi = 0°$, $\theta = 9°$ (the swept case has θ_r slightly below θ_{max}, so a similar choice is made here). As stated, both SCBs have the default $b_{edge} = 0.01c$. Note, of course, that these bumps do not have the same magnitude of performance (Fig. 8), but this is unimportant, since it is the trends in performance which are of interest.

The bumps are re-positioned in discrete intervals to determine their optimal location. As noted earlier, the shock position is affected by the SCB presence; at the current test condition, this tends to result in a small rearward movement. The optimal x_c might then be expected slightly aft of the default $0.48c$ (assuming it occurs for both flows when the shock is 1-3% in front of the crest).

Fig. 14 shows this: peak performance occurs at $0.50c$ for the unswept case, and $0.49c$ for the swept; for both shift of $\pm 0.01c$ gives little performance loss. The difference between the default and optimal x_c, and its effect on $\Delta L/D$, is therefore small, and the use of a sub-optimal default x_c is unlikely to have much impact on other conclusions in the study.

The difference of $0.01c$ between swept and unswept cases matches the small shift in x_{sh} due to boundary layer displacement effects (Section II A), so is presumably more due to the model than any differences in SCB behavior. Inspections of the shock structures support this. In unswept tests, SCBs positioned too far forward see re-expansions over the crest, promoting a double shock system; for those placed too far aft the λ-shock system shrinks in size, reducing the beneficial effect [10, 14, 22]. These same changes are still seen in the swept case, albeit with an asymmetrical shock structure. For both SCBs, a movement forward of optimal sees quite similar rates of fall-off in performance. An aft movement however, which shrinks the shock structure, shows a swifter fall-off for the swept case. This might be due to the manner in which the size of the asymmetrical shock structure changes as it drapes around the repositioned ramp, or perhaps due to the chordwise variation of Λ_{loc}, ψ_{opt} may be a function of the relative positions of the bump and main shock.

B. Isolation Ratio

1. Definition

The isolation parameter, as previously mentioned, characterizes the comparability between 2D SCBs and 3D arrays, and is useful for describing variations in performance. It was first defined by Eastwood and Jarrett [2] as

$$\Phi = 1 - \frac{b_{width} + 2b_{edge}}{b_{spacing}} \tag{2}$$

where for simplicity, 2D bumps have $\Phi = 0$, and the clean wing section $\Phi = 1$. 3D bumps with lower values of Φ are in geometry and behavior more like 2D ones.

It is desirable to establish whether a similar relationship holds for rotated SCBs in swept flow. However, eq. (2) makes no allowance for sweep or orientation. Therefore, an extended definition of isolation, to be termed the effective isolation Φ_{eff}, is sought to remedy this.

To clarify why it is important to include both sweep and rotation, consider first the former, for simplicity assuming an SCB with $\psi = 0°$. The original Φ definition uses the spanwise (LE-parallel) distance between the centre of SCB crests, $b_{spacing}$. From the viewpoint of the oncoming flow, however, the distance between SCB crests is not this measure, but rather its projection perpendicular to the flow direction. Labelling the flow direction as Λ, this projected or 'effective' distance is $b_{s,eff} = b_{spacing} \cos\Lambda$, as illustrated in Fig. 15a.

Now consider the implication of SCB rotation. The spacing $b_{s,eff}$ is not affected by ψ, and so

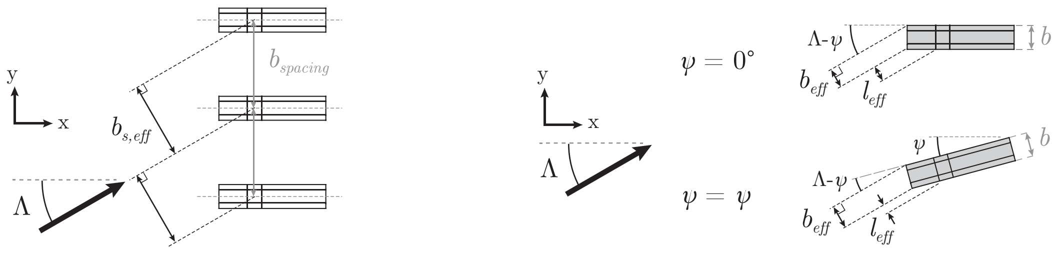

(a) Effective spacing of an array

(b) Effective widths, illustrated for two different SCBs

Fig. 15: Parameters used in Φ_{eff}

the above modification is sufficient for this term. This is not true for the other spanwise dimensions, b_{width} and b_{edge} (combined for simplicity as b). If the SCB has $\psi = 0°$, the 'effective' SCB width as projected perpendicular to the flow is again $b_{eff} = b \cos \Lambda$. However, if $\psi \neq 0°$, from the viewpoint of the oncoming flow (Λ), the width of the SCB depends on the misalignment $\Lambda - \psi$, giving the expression $b_{eff} = b \cos(\Lambda - \psi)$.

Accounting for b_{eff} does not yet give a complete definition of the SCB width normal to the flow direction. If $\Lambda \neq \psi$, the SCB lengths l_{ramp}, l_{crest} and l_{tail} also have contributions to the bump width, which by analogy with b are of the form $l_{eff} = l \sin(|\Lambda - \psi|)$. Individual old and modified terms are illustrated in Fig. 15b.

The issue is then how to include these b_{eff} and l_{eff} terms. Firstly, since the isolation definition is based solely on the footprint of the bump, neither edges, ramp nor tail need to be treated differently, despite differing turning angles. Secondly, and more critically, while all sections of the SCB have some 'width', only those ahead of the shock can help create the λ-structure and resulting drag reduction. The post-shock parts, on the other hand, deal with the boundary layer [27]. They will likely affect drag, but through a different mechanism. Which parts of the SCB (and what proportions of them) are ahead of the shock varies with rotation, so a complete definition for Φ_{eff} should be conditional on ψ, and have the following properties:

1. simplifies to eq. (2) in the case of $\Lambda = \psi = 0°$.

2. accounts for total apparent width of SCB in pre-shock flow (includes b and l terms)

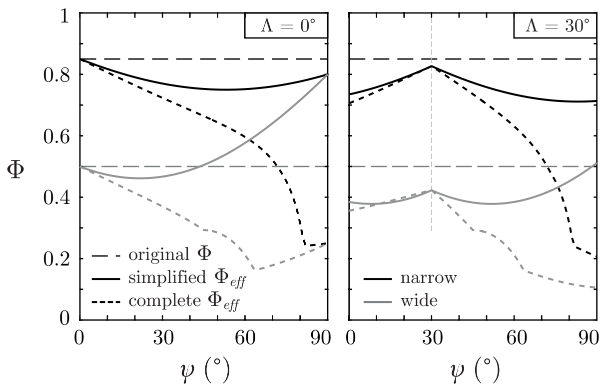

Fig. 16: Example of variation of Φ (–) and Φ_{eff} (-) with ψ.

3. $\Phi_{eff}(\psi = 90°, b, l) = \Phi_{eff}(\psi = 0°, l, b)$

A full conditional definition would be long and complex to notate, so instead a simpler form is written here for illustration: for cases where $\psi << 90°$, and $|\Lambda - \psi|$ is small, contributions from l_{eff} terms are also small, and so writing just $l_{r,eff}$ is sufficiently accurate. Combining the individual modifications, this simplified expression of Φ_{eff} for small rotations and misalignments is

$$\begin{aligned}\Phi_{eff} &= 1 - \frac{b_{w,eff} + 2b_{e,eff} + l_{r,eff}}{b_{s,eff}} \\ &= 1 - \frac{(b_w + 2b_e)\cos(\Lambda - \psi) + l_r \sin(|\Lambda - \psi|)}{b_s \cos\Lambda}\end{aligned} \tag{3}$$

Note that property (1) is satisfied, even for the simplified expression. Fig. 16 shows both the simplified expression and a full definition, to illustrate the differences and range of validity, and does so for swept and unswept flows, and both SCBs considered thus far.

It now remains to determine what the appropriate reference flow direction Λ should be. The logical choice is between the freestream Λ_∞, or some local flow direction Λ_{loc}. Since it is the ramp flow that creates the drag reduction, this is likely the appropriate Λ_{loc}. However, with a change in speed, incidence or aerofoil, any local direction would change, making it unsuitable for defining a geometric parameter. The freestream direction Λ_∞, which is fixed on any given wing, is the rational choice.

2. *Effect on Optimal Rotation*

Before moving on to the main assessment of performance and isolation, it is worth drawing together comments on an earlier issue. In Section III D, changes in effective isolation due to rotation were postulated as one of various factors which may affect the value of ψ_{opt} in cases where interactions with spanwise flows are less significant. Now that Φ_{eff} has been defined, further assessment of whether it is likely to affect ψ_{opt} can be made.

As Fig. 16 illustrates, Φ_{eff} decreases for SCBs misaligned (under or over-rotated) with the reference direction, and so might be assumed to have improved performance, if changes to $\Phi_{eff}(\psi)$ are a significant influence.

This was not observed for the narrow-edged SCB in Section III C, for which performance decreases away from $\psi = 26 - 28°$, reinforcing that the spanwise flows over the edges seem to hold greater importance for this case. Whether or not an isolation effect has a small impact on ψ_{opt} (a few degrees, say) is impossible to ascertain.

This is otherwise for the wide-edged SCB in Section III E. Performance increases for $\psi > 30°$ would be consistent with isolation effects, though decreases for $\psi < 30$ suggests unsurprisingly that isolation effects do not act alone. The spanwise flows are likely to have some influence still, and geometric effects likewise - the position of the start of ramp, around which shock drapes, may well produce a larger λ-footprint for $\psi = 20, 30$ than $0°$, especially so for this wide SCB.

3. *Assessment of Performance Trends*

This final section focuses on the main question regarding isolation: whether the relationship between isolation and peak performance, as observed by [2] for unswept SCB cases, also holds for optimally-rotated narrow-edged SCBs in swept flows. The important assumption here is that, since all designs use the default $b_{edge} = 0.01c$, ψ can be fixed appropriately at $\psi_{opt} = 28°$ (Section III C).

Both swept and unswept cases are tested. All SCB designs (listed in Table 2) use default values other than b_{width}, which is varied to give a range of Φ (eq. 2). The swept designs are produced simply by applying ψ_{opt} to these and calculating $\Phi_{eff}(\Lambda_\infty, \psi_{opt})$ (note that, since $\psi \sim \Lambda_\infty$ and $\psi_{opt} << 90°$, the simplified expression in eq. 3 is appropriate.) Using a rotation of $28°$ places

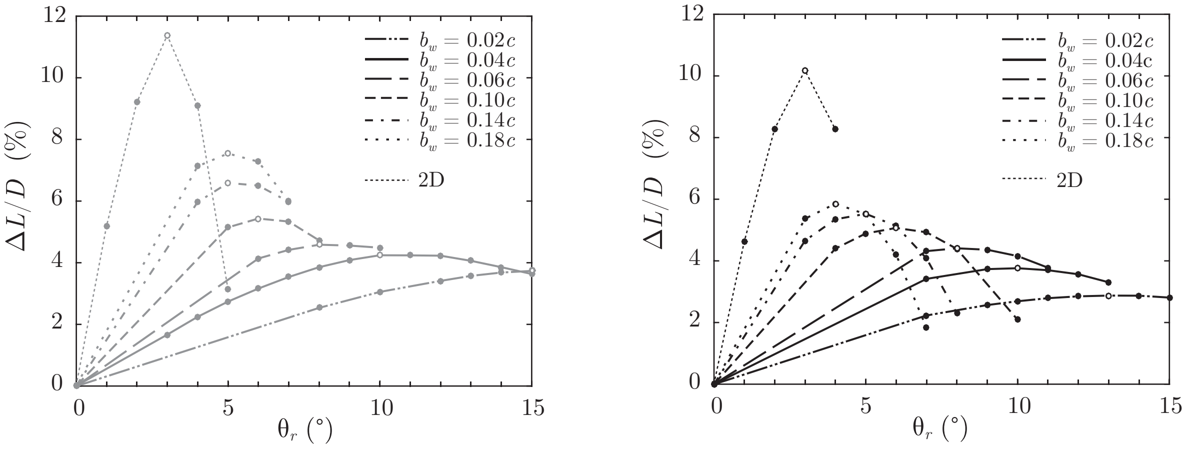

(a) $\Lambda_\infty = \psi = 0°$

(b) $\Lambda_\infty = 30°$, $\psi = 28°$

Fig. 17: Variation of performance with b_{width} ($b_{edge} = 0.01c$)

a lower limit on the value of Φ which can be tested, for the same reasons given for limiting ψ in Section III E. This lower limit is taken as $\Phi = 0.5$ - the same value as the wide-edged SCB. Each SCB is tested over a limited range of θ_r as sufficient to determine L/D_{max}.

2D SCB cases are also included for comparison. Of these, unswept cases use a simple 2D aerofoil mesh, with a 2D SCB using the default chordwise parameters; the swept cases use similar, with the mesh extended spanwise by $0.05c$.

Fig. 17 shows the results as a function of width, whilst Fig. 18 compares L/D_{max} for each SCB against the two isolation definitions. The 2D cases exhibit the expected results: similar shapes (θ_r),

Table 2: SCB parameters for isolation study. Φ_{eff} listed for $\Lambda_\infty = 30°$, $\psi = 28°$

x_c	b_{edge}	$b_{spacing}$	b_{width}	Φ	Φ_{eff}
			$0.02c$	0.90	0.877
			$0.04c$	0.85	0.819
			$0.06c$	0.80	0.761
$0.48c$	$0.01c$	$0.40c$	$0.10c$	0.70	0.646
			$0.14c$	0.60	0.530
			$0.18c$	0.50	0.425

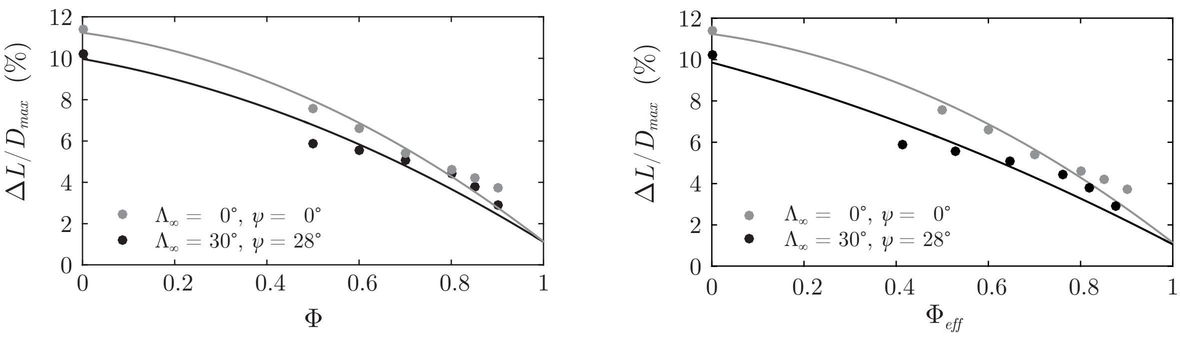

(a) Original Φ definition (eq. 2).

(b) Φ_{eff} definition (eq. 3) (includes Λ and ψ).

Fig. 18: Isolation versus maximum performance

with lower performance in swept flow due to the smaller contribution of pressure/wave drag to the total [4]). For the 3D SCBs, the overall trend for both swept and unswept cases is that wider (less isolated) bumps act more like 2D SCBs, having higher L/D_{max} and smaller θ_{max}. This is therefore in general agreement with the unswept trends of [2]. The unswept trend line is also of similar shape to that obtained by [2] for a different aerofoil and flow condition.

The swept data does show some differences, however. The narrowest bump sees weaker performance, and similarly as the SCBs get less isolated, more strongly diminishing returns are observed. It seems therefore, that whilst a similar trend between isolation and performance is seen for narrow-edged SCBs with fixed rotation, this is not consistently sufficient for obtaining a maximum performance curve comparable to the unswept case. Thus there are two possibilities. Either rotation is less successful for wider but narrow-edged SCBs, or the assumption that the optimal rotation of narrow, narrow-edged bumps is applicable for all b_w is not valid. Further work might be required to seek the dependency of ψ_{opt} on both b_w and b_e, and then establish whether a maximum performance curve more similar to the unswept one can be obtained by varying ψ and Φ in conjunction.

As previously discussed, the maximum performance of swept SCBs would be expected to be lower than unswept. From this view, the new definition of isolation shows a better description: particularly around $\Phi_{eff} = 0.8$, where the correct ψ_{opt} is known, Φ_{eff} seems to provide a somewhat better delineation between swept and unswept data.

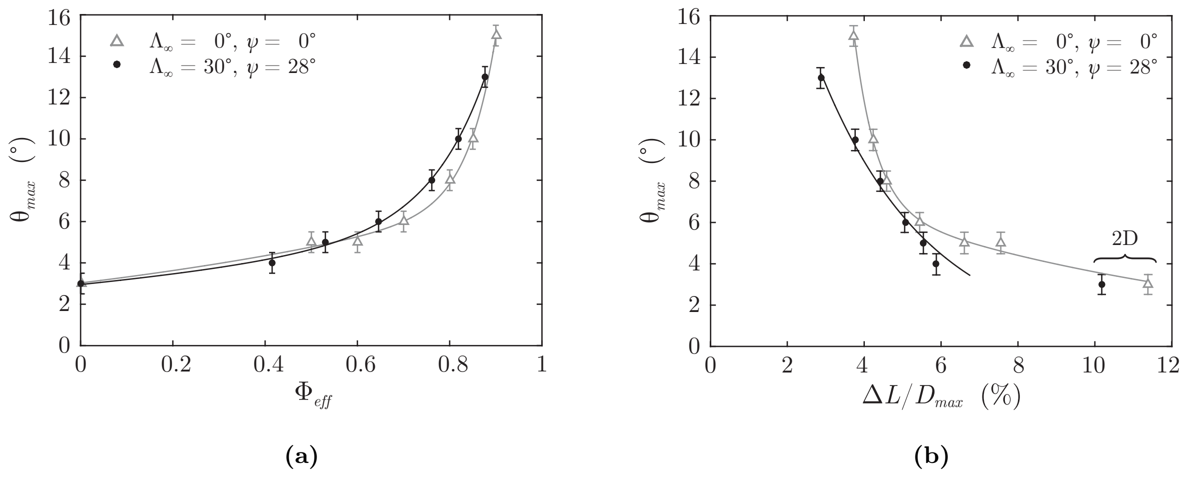

Fig. 19: Comparison of θ_{max} with Φ_{eff} and corresponding peak performance.

C. Optimal Ramp Angle

The final useful comparison between swept and unswept bumps is that of the optimal ramp angle required to achieve the performances in Fig. 18. θ_{max} as a function of both isolation and L/D_{max} is presented in Fig. 19. Firstly, this illustrates what has already been stated: in both flows more isolated SCBs need a higher θ_r and have a lower L/D_{max}.

More interestingly, the values of θ_{max} are similar between the two data sets, though not identical. Comparing SCBs of similar Φ_{eff} shows that between $\Phi_{eff} \simeq 0.6 - 0.85$ the swept cases tend to require a θ_r of $1 - 2°$ taller, whilst towards low and the highest Φ_{eff}, values of θ_{max} are much closer. This range of Φ_{eff} where θ_{max} differs also seems to correspond to the range where the gap in performances between swept and unswept SCBs is smallest, so might be related to a correct selection of ψ_{opt}. The increase in θ_{max} required for comparable performance could feasibly be related to the misalignment with the ramp flow ($\Lambda_{loc,ramp} = 20°$, $\psi_{opt} = 28°$) which may encourage more flow to spill off the ramp than in an equivalent unswept case with a symmetrical ramp flow. Hence a larger θ_{ramp} is required to achieve a the respective maximum levels of flow turning.

From the plot in Fig. 19b of performance against θ_{max}, it can be observed that the fall off in performance at the more isolated, higher θ_{max} end of the curve is associated with a slower rate of increase in θ_{max}. That very tall SCBs do not do so well in swept flows accords with the earlier discussions on ψ_{opt}: higher θ_r implies greater sensitivity to the spanwise flows, and hence to the SCB orientation and any small deviation from optimum. It would therefore seem a reasonable inference that θ_r for swept SCBs cannot be indefinitely increased to compensate for increasing isolation. The final θ_{max} would be the mediation of an increase as compensation for high isolation, and a decrease to alleviate the subsequent re-expansions over the SCB edges (see Section III B).

At the low θ_{max}, less isolated end of the curve, the performance differences as discussed might be due to a dependency of ψ_{opt} on b_w as well as b_e, though whether this would be sufficient to close the performance gap for less isolated SCBs is not known. It is also worth noting that additional tests varying ψ for the wider bumps would be unlikely to significantly alter the values of θ_{max}: since for the wider SCBs θ_{max} is low, less sensitivity of θ_{max} to ψ would be expected, particularly away from extreme values of ψ (eg: $0, 90°$). This pattern is already seen for the wide-edged SCB (Fig. 12, $\psi = 20 - 40°$), so whilst more sensitivity would be expected due to sharper edges, this earlier test gives some indication of what to expect.

V. Limitations of the Study

Due to finite resources, there are several limitations to the work presented here. Firstly, the results represent one test condition and one value of Λ_∞, with many of the SCB geometric parameters held fixed. Hence values of ψ_{opt} might not relate to more general flow conditions on arbitrary aerofoils. Secondly, for SCB designs significantly affected by the spanwise flow, nothing can be said on the potential variation of ψ_{opt} along a finite swept wing, due to changes in Λ_{loc} as well as the shock position and strength. Thirdly, it is possible that in swept flows, contour bumps, newer geometries such as extended-SCBs (eg: [27, 30]), or very different shapes entirely might be better suited than wedge bumps. Lastly, due to the inherent limitations of RANS codes particularly in dealing with post-shock flows, little consideration has been given in this paper to flow physics around SCBs. Future work will aim to remedy this using higher-fidelity CFD, namely hybrid LES on select cases, which would be better suited for such analyses and for verification of the presented results.

VI. Conclusion

A numerical investigation was performed to examine the effect of swept flows on the design-point drag performance of 3D shock control bumps, using an infinite swept wing model with a turbulent transonic aerofoil section. The study aimed to address the questions of firstly, how this performance compared to that of SCBs in unswept flows, and secondly, how the performance was affected by a new variable of SCB orientation (here simple rotation).

To answer question one, the drag performance as a function of key design variables was assessed, and the following conclusions were drawn:

- Chordwise position has the same influence in swept and unswept flows. The optimal position is similar, to within about $0.01c$, and is still with the shock 1-3% in front of the crest.
- An extended definition of SCB isolation, Φ_{eff}, was constructed to account for apparent changes due to sweep and rotation.
- The degree of isolation of SCBs also has similar influence, with less isolated bumps achieving higher maximum performance while requiring lower ramp angles θ_{max} to achieve it.
- However, varying isolation (here through b_w) for SCBs of fixed ψ does not produce a performance-isolation curve of the same shape as in unswept flows. It is possible that ψ must also be varied with isolation in order to obtain best performance.
- The values of θ_{max} required for swept and unswept SCBs of comparable Φ_{eff} are similar and follow similar trends, though over a range of $\Phi_{eff} \simeq 0.6 - 0.85$, swept bumps must have θ_r $1 - 2°$ higher.

The attempt to answer question two led to an investigation of the optimal rotation ψ_{opt} for two different SCBs. Orientation was found to have a strong impact on swept-flow performance, with a clearly optimal value required to achieve performance similar to that possible in unswept flows. For a classically shaped 3D SCB (fairly narrow, with narrow edges), ψ_{opt} was found to be $26 - 28°$. This value was not much dependent on the SCB ramp angle, although θ_r did strongly affect the sensitivity to rotation. The performance of short bumps is not heavily afflicted by rotation away from the optimal value, but for tall bumps, where the height exacerbates the detrimental effect of the spanwise flows, performance is more strongly dependent on orientation. The value of ψ_{opt} appears to correspond to aligning the SCB with an average of the local flow direction in its vicinity, which mitigates the worst of the effects of the inevitable spanwise flows across the bump's narrow edges.

For a non-classical SCB (wide sloping edges), other influences play an increasing role in how rotation affects performance. The optimal rotation was found to be much higher, though undetermined. It was proposed that, in this case where spanwise flow across the bump edges has a more moderate effect, changes in the apparent degree of isolation due to ψ, as well as other geometric effects, may be more significant. The total width of the bump, as well as the width of the edges, may therefore be important.

These are useful findings, because they show that an adjustment to SCB orientation could be used to adapt classic, unswept 3D SCBs for use in an equivalent swept flow. For classically shaped SCBs (narrow; narrow edges) simple rules can be followed: retain x_c, rotate the SCB to align roughly with the local flow direction, and test small variations in θ_r of $1 - 2°$ to find the optimum. This method has some use for wider, narrow-edges SCBs, though further work is required to check the correct alignment. These findings also have implications for the use of SCBs in other applications featuring swept flows, such as those found in some engine intakes.

Future work will aim to investigate further how SCB geometry and sweep affect optimal rotation, as well as the off-design behaviour of rotated SCBs, including the implication for vortex generation and any trade-off between design drag and off-design buffet performance.

Acknowledgments

The authors would like to thank the United Kingdom Engineering and Physical Sciences Research Council for funding the research. The raw data underlying this publication comprises over 200 numerical simulations, each consisting of multiple data files. These raw files are not shared online due to size (up to 1GB/case); public sharing is not cost-efficient, and the experiment can be easily reproduced using the information in the Methods section. Instead, this publication is accompanied by a reduced set of data, as obtained from post-processing procedures in order to perform the analyses presented (see: http://dx.doi.org/10.17863/CAM.417).

References

[1] Ashill, P. R., Fulker, J. L., and Shires, A., "A Novel Technique for Controlling Shock Strength of Laminar-Flow Aerofoil Sections," DGLR-Bericht 92-01, 1992.

[2] Eastwood, J. P. and Jarrett, J. P., "Toward Designing with Three-Dimensional Bumps for Lift/Drag Improvement and Buffet Alleviation," *AIAA Journal*, Vol. 50, 2012, pp. 2882–2898, doi:10.2514/1.J051740.

[3] Stanewsky, E., Délery, J. M., Fulker, J. L., and de Matteis, P., "Synopsis of the Project EUROSHOCK II," in "Notes on Numerical Fluid Mechanics and Multidisciplinary Design: Drag Reduction by Shock and Boundary Layer Control: Results of the Project EUROSHOCK II," Springer-Verlag Inc, Vol. 80, pp. 1–124, 2002.

[4] Kutzbach, M., Lutz, T., and Wagner, S., "Investigations on Shock Control Bumps for Infinite Swept Wings," in "2nd AIAA Flow Control Conference," Portland, OR, USA, 2004, doi:10.2514/6.2004-2702.

[5] König, B., Pätzold, M., Lutz, T., Krämer, E., Rosemann, H., Richter, K., and Uhlemann, H., "Numerical and Experimental Validation of Three-Dimensional Shock Control Bumps," *Journal of Aircraft*, Vol. 46, 2009, pp. 675–682, doi:10.2514/1.41441.

[6] Milholen, W. and Owens, L., "On the Application of Contour Bumps for Transonic Drag Reduction (Invited)," in "43rd AIAA Aerospace Sciences Meeting and Exhibit," Reno, Nevada, 2005, doi:10.2514/6.2005-462.

[7] Wong, W. S., Qin, N., Sellars, N., Holden, H., and Babinsky, H., "A Combined Experimental and Numerical Study of Flow Structures Over Three-Dimensional Shock Control Bumps," *Aerospace Science and Technology*, Vol. 12, 2008, pp. 436–447, doi:10.1016/j.ast.2007.10.011.

[8] Ashill, P. R., Fulker, J. L., and Simmons, M. J., "Simulated Active Control of Shock Waves in Experiments on Aerofoil Models," in "Second International Conference of Experimental Fluid Mechanics," Turin, Italy, 1994.

[9] Ogawa, H. and Babinsky, H., "Evaluation of Wave Drag Reduction by Flow Control," *Aerospace Science and Technology*, Vol. 10, No. 1, 2006, pp. 1–8, doi:10.1016/j.ast.2005.08.001.

[10] Ogawa, H., Babinsky, H., Paetzold, A., and Lutz, T., "Shock-Wave/Boundary-Layer Interaction Control Using Three-Dimensional Bumps for Transonic Wings," *AIAA Journal*, Vol. 46, 2008, pp. 1442–1452,

doi:10.2514/1.32049.

[11] Sommerer, A., Lutz, T., and Wagner, S., "Numerical Optimisation of Adaptive Transonic Airfoils with Variable Camber," in "Proceedings of the 22nd International Congress of the Aeronautical Sciences," Harrogate, UK, 2000.

[12] König, B., Pätzold, M., Lutz, T., and Krämer, E., "Shock Control Bumps on Flexible and Trimmed Transport Aircraft in Transonic Flow," in "New Results in Numerical and Experimental Fluid Mechanics VI," Springer, Berlin, Heidelberg, Vol. 96 of *Notes on Numerical Fluid Mechanics and Multidisciplinary Design (NNFM)*, pp. 80–87, 2008,
doi:10.1007/978-3-540-74460-3.

[13] Holden, H. and Babinsky, H., "Shock / Boundary Layer Interaction Control Using 3D Devices," in "41st Aerospace Sciences Meeting and Exhibit," American Institute of Aeronautics and Astronautics, 2003,
doi:doi:10.2514/6.2003-44710.2514/6.2003-447.

[14] Bruce, P. J. K. and Babinsky, H., "Experimental Study into the Flow Physics of Three-Dimensional Shock Control Bumps," *Journal of Aircraft*, Vol. 49, No. 5, 2012, pp. 1222–1233,
doi:10.2514/1.C031341.

[15] Qin, N., Wong, W. S., and Le Moigne, A., "Three-Dimensional Contour Bumps for Transonic Wing Drag Reduction," *Proceedings of the Institution of Mechanical Engineers*, Vol. 222, No. Part G: J. of Aerospace Engineering, 2008, pp. 619–629,
doi:10.1243/09544100JAERO333.

[16] Babinsky, H. and Ogawa, H., "SBLI Control for Wings and Inlets," *Shock Waves*, Vol. 18, No. 2, 2008, pp. 89–96,
doi:10.1007/s00193-008-0149-7.

[17] Bruce, P. J. K. and Colliss, S. P., "Review of Research Into Shock Control Bumps," *Shock Waves*, Vol. 25, No. 5, 2014, pp. 451–471,
doi:10.1007/s00193-014-0533-4.

[18] Kim, S. D., "Aerodynamic Design of a Supersonic Inlet with a Parametric Bump," *Journal of Aircraft*, Vol. 46, No. 1, 2009, pp. 198–202,
doi:10.2514/1.37416.

[19] Zhang, Y., Tan, H.-j., Sun, S., and Rao, C.-y., "Control of Cowl Shock/Boundary-Layer Interaction in Hypersonic Inlets by Bump," *AIAA Journal*, Vol. 53, No. 11, 2015, pp. 3492–3496,
doi:10.2514/1.J053974.

[20] Birkemeyer, J., Rosemann, H., and Stanewsky, E., "Shock Control on a Swept Wing," *Aerospace Science*

and Technology, Vol. 4, 2000, pp. 147–156,
doi:10.1016/S1270-9638(00)00128-0.

[21] Pätzold, M., Lutz, T., Krämer, E., and Wagner, S., "Numerical Optimization of Finite Shock Control Bumps," in "44th AIAA Aerospace Sciences Meeting and Exhibit," Reno, Nevada, 2006, doi:10.2514/6.2006-1054.

[22] Eastwood, J. P., *3D Bumps : Bridging the Gap Between Lift/Drag Improvement and Buffet Alleviation?*, Ph.D. thesis, University of Cambridge, 2012.

[23] Rodde, A. M. and Archambaud, J. P., "OAT15A Airfoil Data," in "A Selection of Experimental Test Cases for the Validation of CFD Codes, AGARD-AR-303, Vol. 2," 1994, pp. A11:1–13.

[24] Reshotko, E. and Beckwith, I. E., "Compressible Laminar Boundary Layer Over a Yawed Infinite Cylinder with Heat Transfer and Arbitrary Prandtl Number," Report 1379, NACA, 1958.

[25] Lindfield, A.W., Pinsent, H.G. and Pinsent, P.A., "Approximate Methods for Calculating Three-Dimensional Boundary Layer Flow on Wings", *Boundary Layer and Flow Control: Its Principles and Application*, edited by Lachmann, G.V., Vol. 2, Pergamon Press, London, 1961.

[26] Thompson, B. G. J. and Macdonald, A. G. J., "The Prediction of Boundary-Layer Behaviour and Profile Drag for Infinite Yawed Wings: Part I A Method of Calculation," C.P. No. 1309, Aeronautical Research Council, 1974.

[27] Colliss, S. P., *Vortical Structures on Three-Dimensional Shock Control Bumps*, Ph.D. thesis, University of Cambridge, 2014.

[28] ANSYS Inc., "ANSYS Fluent User's Guide 15.0," 2013.

[29] Dandois, J., Molton, P., Lepage, A., Geeraert, A., Brunet, V., Dor, J.-B., and Coustols, E., "Buffet Characterization and Control for Turbulent Wings," *AerospaceLab: The ONERA Journal*, Vol. 6.

[30] Mayer, R., Lutz, T., and Krämer, E., "Toward Numerical Optimization of Buffet Alleviating Three-Dimensional Shock Control Bumps," in "6th European Conference For Aerospace Sciences," Krakow, Poland, 2015.

[31] Deck, S., "Numerical Simulation of Transonic Buffet over a Supercritical Airfoil," *AIAA Journal*, Vol. 43, No. 7, 2005, pp. 1556–1566,
doi:10.2514/1.9885.

[32] Jacquin, L., Molton, P., Deck, S., Maury, B., and Soulevant, D., "Experimental Study of Shock Oscillation over a Transonic Supercritical Profile," *AIAA Journal*, Vol. 47, No. 9, 2009, pp. 1985–1994,
doi:10.2514/1.30190.

[33] Spalart, P. R. and Allmaras, S. R., "A One-Equation Turbulence Model for Aerodynamic Flows," *La*

Recherche Aerospatiale, Vol. 1, 1994, pp. 5–21.

[34] Brunet, V., "Computational Study of Buffet Phenomenon with Unsteady RANS Equations," in "21st AIAA Applied Aerodynamics Conference," AIAA, Orlando, Florida, 2003, doi:10.2514/6.2003-3679.

[35] Colliss, S. P., Babinsky, H., Nübler, K., and Lutz, T., "Joint Experimental and Numerical Approach to Three-Dimensional Shock Control Bump Research," *AIAA Journal*, Vol. 52, No. 2, 2014, pp. 436–446, doi:10.2514/1.J052582.

[36] ANSYS Inc., "ANSYS Meshing Help 12.1," 2009.